

Qinhong Fan
Hongwei Gao ✉
Zhibing Chu
Yuxin Zhang
Yanan Cui
Wenze Wang

<https://doi.org/10.21278/TOF.462036921>
ISSN 1333-1124
eISSN 1849-1391

HOT COMPRESSION TEST AND MICROSTRUCTURE EVOLUTION IN LZ50 AXLE STEEL

Summary

True strain-true stress curves of the LZ50 axle steel were obtained after hot compression tests had been performed on a Gleeble-3800 thermal simulator at strain rates of 0.01, 0.1, 1 and 5 s⁻¹ and at deformation temperatures from 850 to 1,150 °C. Following the data processing, the relationship between the flow stress and the deformation temperature of the material under different true strain conditions was analysed. On this basis and according to the influence of deformation factors, the constitutive equation of the Johnson-Cook flow stress model is established, and the model is modified according to the defects of the model, so that the improved model can effectively predict the mechanical behaviour in the range of high strain rates and temperatures. The dynamic material model (DMM) was used to generate the hot working diagram of the material. Through calculation and analysis, the optimum process area in terms of temperature was found to be in the range from 1,050 to 1,150 °C and in terms of strain rate in the range from 1 to 5 s⁻¹. Finally, the microstructure evolution of the compressed specimens under different strain rates and temperatures was studied in the metallographic analysis, which provided a theoretical basis and reference value for later damage.

Key words: LZ50 axle steel, hot compression, constitutive model, hot working diagram

1. Introduction

Rail transit is a key development field in China's manufacturing industry. At present, China is promoting the construction of the "eight vertical and eight horizontal" high-speed railway network. At the same time, China also actively promotes the modal shift of bulk cargo from road to rail. According to *The research report on the supply and demand status and investment risk of the high-speed railway wheel axle industry in China during the 13th Five-Year Plan (2016-2020)*, the demand for high-speed railway wheel axles in China at the present stage is satisfied. Table 1 shows the demand for railway axles in China during the 13th Five-Year Plan period. Until the end of 2020, the total length of China's high-speed railways in operation exceeded 35,000 km, ranking first in the world and accounting for well over two-

thirds of the world's total [1]. On the one hand, the increase in the total mileage of high-speed railway in operation has brought convenience in travel to work and in general, on the other hand, the transportation safety of high-speed railway has been increasingly causing concern.

Table 1 Axle requirements for railway vehicles during the 13th Five-Year Plan period

Axle types	New vehicles	Vehicle care	Total requirements
Truck axle	50,000	40,000	360,000
Bus axle	1,250	1,250	10,000
Bullet train axle	3,240	2,700	23,760
Locomotive axle	1,500	70,700	46,800
Urban rail axle	3,600	10,000	54,400
Engineering axle	5,000	1,250	25,000
Total	64,590	125,900	519,960

Axle steel is an important bearing part of the high-speed train bogie, and its performance changes during the transportation process. It also affects the safety of train transportation [2, 3, 4]. Fracture of any axle will often lead to train breakdown, transportation interruption and even fatal accidents. Fig. 1 shows the service life distribution curve of axles broken due to fatigue. As can be seen from the figure, the lifetime of a train axle is 6-21 years. Therefore, in order to prevent the occurrence of axle fracture accidents, but also to protect the safety of personnel and property, the study on mechanical properties of axles has major significance for the long-term development of rail transportation and railway industry.

Yang Dawei et al. [5] studied the deformation behaviour of PH13-8Mo steel under hot compression, and obtained a characteristic curve of the true stress rising first, then flattening and finally continuing to rise in the process of hot compression deformation. They also established a constitutive model of hot deformation of the PH13-8Mo steel using the Zhou Jihua-Guan Kezhi model in the simulation process. Jin Xueqin et al. [6] studied the thermal compression dynamic microstructure evolution of the P91 steel by using a thermal simulator, conducted a numerical simulation in the FEM software DEFORM, and found that the simulated value was basically consistent with the measured value. Zhang Yonggang et al. [7] used a Gleeble-3500 thermal simulator to carry out thermal compression on cylinder samples, studied the rheological curve of the materials, and then corrected the distortion of the stress-strain curve caused by friction to make the rheological curve closer to the actual situation. Sun Zhiren et al. [8] established a dynamic recrystallization model of the 40Mn steel and verified it in the Gleeble hot compression experiment. Wu Shuting et al. [9] studied the rheological behaviour and microstructure evolution of the 20CrMnTiH steel under hot compression and analysed the flow deformation behaviour of the material.

J. Bennetta et al. [10] used a Gleeble thermo-mechanical simulator to conduct a thermo-mechanical coupling finite element simulation of the isothermal axisymmetric compression test, so as to compare a possible relative stress error level in each test. They also evaluated test methods and calculated relative errors by providing a reference stress-strain curve. Ahmad Chamanfar et al. [11] studied the hot deformation behaviour of the newly developed AA6099 alloy after the homogenisation treatment and determined the relationship among the flow behaviour, different microstructure and dynamic softening mechanism under different hot compression conditions. Y. Gajalappa et al. [12] carried out a thermal compression test on an Inconel alloy based on a Gleeble-3800 thermal simulation machine and drew a true stress-strain curve by using thermal compression data. H. Xiao et al. [13] established a thermoelectric and

mechanical coupling finite element model of the thermal compression of the TA15 titanium alloy using a Gleeble thermal simulation system and achieved an accurate temperature control through a negative feedback control algorithm. Qiang Li et al. [14] corrected the real stress and strain of powder metallurgy steel in a Gleeble thermal tensile test, proposed a high-temperature fracture strain model of powder metallurgy steel based on the Zener-Hollomon parameter, and established the Cockroft and Latham fracture criterion coupled with thermal processing parameters.

Kun Dou et al. [15] conducted isothermal compression tests on the YQ450NQR1 low carbon (wt. 0.12%) vanadium microalloying steel in the temperature range from 1,143 K to 1,433 K by using a Gleeble-1500 thermal simulator and obtained a flow stress curve of the YQ450NQR1 steel. Based on the experimental stress-strain data, a constitutive model considering deformation activation energy was established. S.H. Adarsh et al. [16] used a Gleeble-3800 thermal simulation device and a dynamic material model (DMM) to generate a processing diagram containing efficiency diagram and instability diagram. Siegfried Kleber et al. [17] used the Gleeble test to conduct hot compression tests on cylindrical specimens and simulated them using the finite element method. By introducing a friction and temperature gradient, corresponding local strain changes of bulging edges were reduced. X. Wang et al. [18] proposed a reverse method combined with the finite element analysis to modify the experimental stress-strain curve and obtain an actual stress-strain curve of the material. D.J. Yu et al. [19] simulated the Gleeble compression process of a titanium alloy (Ti60) sample by using the thermo-mechanical coupling finite element method and compared the obtained results with the actual compression test results obtained from a Gleeble-3800 thermo-mechanical simulator. Based on the finite element simulation and iterative correction, a method to improve the Gleeble test constitutive relation is proposed.

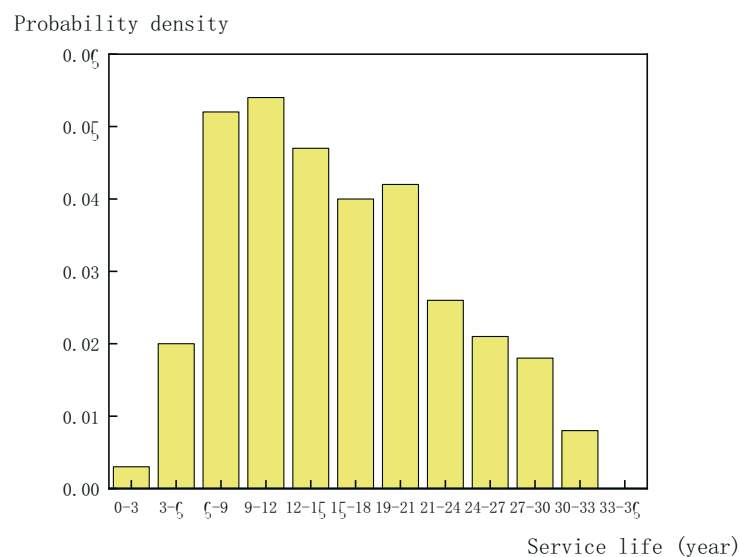


Fig. 1 Distribution curve of railway axle life

2. Materials and methods

2.1 Test material composition

In this test, the LZ50 axle steel is used as the test material. The chemical composition of the LZ50 axle steel was obtained from the spectral analysis, as shown in Table 2. By referring to literature [20, 21] the main mechanical properties of the LZ50 axle steel are obtained, as shown in Table 3.

Table 2 Chemical composition of LZ50 axle steel (% mass fraction)

Chemical element	C	Si	Mn	P	S	Cr
Mass fraction	0.53	0.26	0.76	0.011	0.002	0.22
Chemical element	Ni	Cu	V	As	Sn	Alt
Mass fraction	0.020	0.031	0.024	0.004	0.002	0.029

Table 3 Main mechanical properties of LZ50 axle steel

Mechanical properties	$\sigma_{0.2}$ (MPa)	σ_b (MPa)	E (GPa)	HV
LZ50	375	650	210	245-265

2.2 Experimental setup

In this test, a Gleeble-3800 thermal simulation test machine (as shown in Fig. 2) was used to conduct a hot compression test on the LZ50 axle cylindrical steel sample with a diameter of 10 mm and height of 15 mm the sample had been ground and polished. The cylindrical sample is shown in Fig. 3.



Fig. 2 Gleeble-3800 thermal simulation test machine



Fig. 3 Axle steel cylinder

The preparation steps are as follows: graphite sheets are evenly attached to both ends of the Gleeble-3800 thermal simulator coupling to provide lubrication and prevent the sheets from sticking to the anvil during heating; the two ends of the cylindrical specimen are glued with shrapnel to reduce friction, thus reducing the uneven deformation to the greatest extent; through the fixture into the experimental cabin door, the cylindrical sample must be put into the middle position of the coupling and clamped to make sure that the clamping is moderate; after confirming that the sample and measuring instrument are installed correctly, the fixture is taken out, the door of the experimental chamber is closed, and the air is pumped out to achieve a vacuum environment.

The formal steps are as follows: the cylindrical sample is heated to 1,250 °C at a heating rate of 10 °C/s, kept at this temperature for 3 min and cooled to four different deformation temperatures by water cooling and kept for 1 min to obtain uniform structure; thermal compression tests are carried out on cylindrical specimens with deformation temperatures of 850, 950, 1,050 and 1,150 °C and strain rates of 0.01, 0.1, 1 and 5 s⁻¹, respectively. The total pressure reduction was 60% (the maximum true strain was 0.916).

2.3 Test curve

For the hot compression forming of the axle steel the four deformation temperatures of 850, 950, 1,050 and 1,150 °C were selected from the deformation temperature range from 800 to 1,200 °C, and the hot deformation samples were retained by cooling with water rapidly after hot compression. The testing scheme is shown in Fig. 4.

When the Gleeble hot compression is performed on a sample, it should be noted that the sample thermocouple can accurately detect the temperature. If the temperature of the monitoring panel is abnormal, the hot compression test should be stopped immediately, then the residual material in the cabin should be cleaned, and the cylindrical sample should be replaced for the hot compression test.

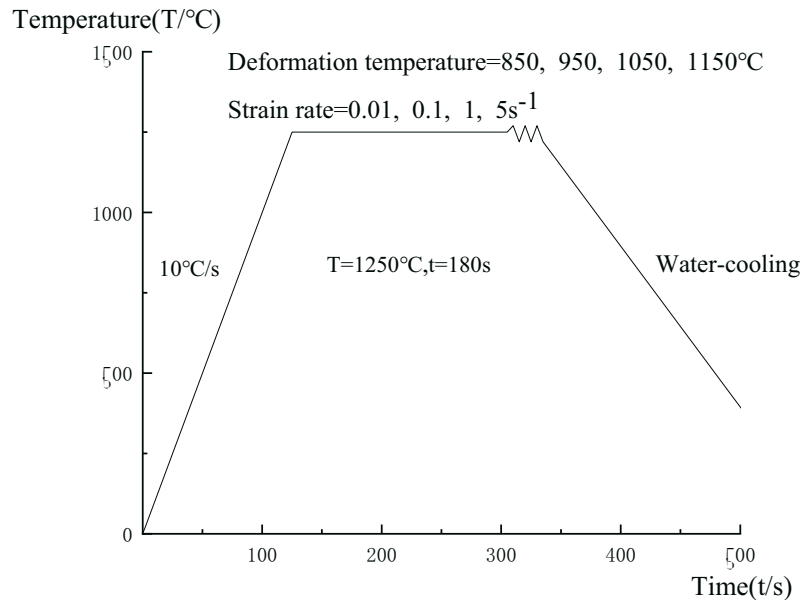


Fig. 4 Thermal simulation testing scheme of axle steel

3. Analysis of test results

3.1 Stress-strain curve analysis

3.1.1 True stress-true strain curve analysis

After the test, the hot compressed test samples were archived, as shown in Table 4. For example, "0.01-850" refers to the hot compressed sample under the condition of the strain rate of 0.01 s^{-1} and the deformation temperature of $850 \text{ }^\circ\text{C}$.

The Origin software is used to analyse and process the test data. According to the X (strain) and Y (stress) coordinate points corresponding to the data and according to the formula for the calculation of true strain and true stress, the corresponding coordinate points can be solved and the original curve can be obtained, and then the true stress-strain curve can be drawn after fitting. Fig. 5 shows the true stress-strain curves at different rates.

The true strain (ϵ) and true stress (s) can be calculated as follows:

$$\epsilon = -\ln(1 - \epsilon) \tag{1}$$

$$s = \sigma(1 - \epsilon). \tag{2}$$

where ϵ is the strain of the original data, and σ is the stress of the original data.

It can be seen from Fig. 4 that the true stress-true strain curve of the LZ50 axle steel at different strain rates shows that the true stress increases rapidly at the initial stage with a constant increase in the true strain, then the true stress decreases at the middle stage and gradually flattens at the later stage. The analysis shows the following three main facts:

Table 4 Hot compressed samples

0.01-850 	0.01-950 	0.01-1050 	0.01-1150 
0.1-850 	0.1-950 	0.1-1050 	0.1-1150 
1-850 	1-950 	1-1050 	1-1150 
5-850 	5-950 	5-1050 	5-1150 

(1) When the deformation temperature is lower (suppose $T=850\text{ }^{\circ}\text{C}$) and the strain rate is higher (suppose $\dot{\epsilon}=5\text{ s}^{-1}$), the true stress changes more rapidly with the true strain value, and the stress-strain curve at this point shows a dynamic recovery type characteristic, which is related to the dislocation climbing which is in turn related to internal dislocation slip or diffusion. Moreover, the deformation time will shorten during this deformation stage, making it impossible for the dynamic recovery to completely eliminate the distortion caused by the dislocation slip in the material.

(2) When the deformation temperature is higher (suppose $T=1,150\text{ }^{\circ}\text{C}$) and the strain rate is lower (suppose $\dot{\epsilon}=0.01\text{ s}^{-1}$), the true stress tends to be flat with the change in the true strain value, and the stress-strain curve at this point presents a dynamic recrystallisation type characteristic. The reason for this is that at the initial stage of deformation, the density of dislocation increases rapidly, resulting in the strain hardening of the material. However, the softening caused by the dislocation slip is not sufficient to counteract the hardening of the material. Therefore, with an increase in strain, a large amount of distortion energy is accumulated in the material, which begins to show dynamic recrystallisation characteristics [22].

(3) On the whole, the deformation resistance of the LZ50 axle steel decreases with the increase in the deformation temperature when the strain rate is the same, which is unfavourable for the thermal deformation of the material. Therefore, the selection of an appropriate thermal deformation temperature has a vital influence on the improvement of the performance of the axle steel.

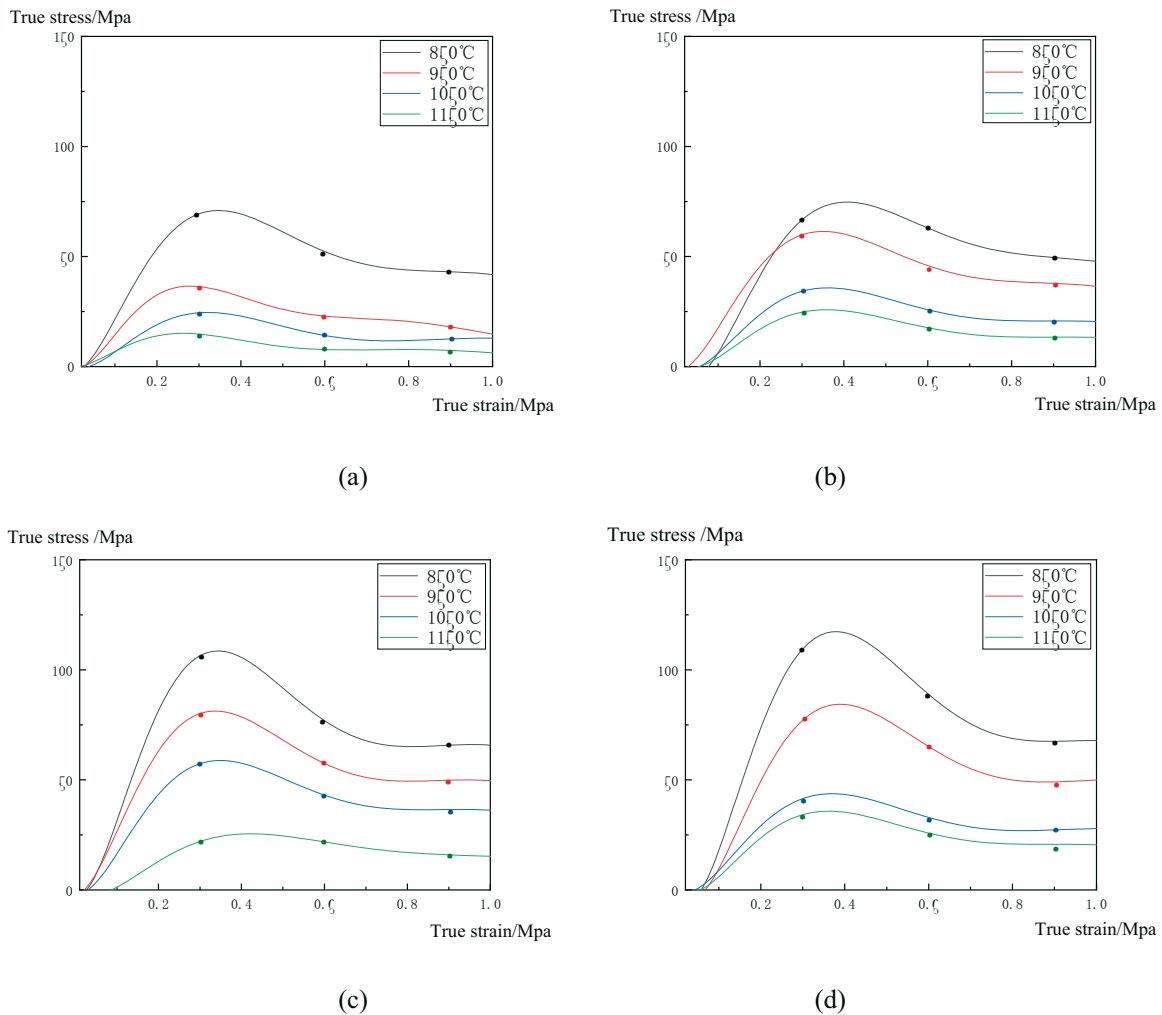


Fig. 5 True stress-true strain curve of LZ50 axle steel at different strain rates
0.01 s⁻¹ (b) 0.1 s⁻¹ (c) 1 s⁻¹ (d) 5 s⁻¹

In summary, according to relevant studies proposed by other researchers [23, 24, 25] the typical flow stress of metals will go through three stages, namely work hardening, dynamic recovery and dynamic recrystallisation. With the change in strain rate and deformation temperature, the specific curve shape will change correspondingly. From the true stress-true strain behaviour of the whole LZ50 axle steel, the initial stage is characterised by strain hardening, and the variable stress increases linearly with the strain. This linear increase in stress is due to dislocation generation, dislocation proliferation or dislocation density increase. As the temperature rises, the generation of dislocations is counteracted by some other mechanism, namely dislocation recovery, due to the concentration of vacancies in the material that balances the generation of dislocations that lead to state behaviour.

3.1.2 Analysis of flow stress curve

Based on the true stress-strain curve analysis, the relationship curves between the flow stress and the deformation temperature under different true strains were drawn, as shown in Fig. 6. Compared with the true stress-strain curve, the flow stress decreases with the increase in the

deformation temperature when the strain rate is constant. In addition, it can be seen from the three groups of graphs that when the deformation rate is 0.01 s^{-1} , the change in the flow stress shows a slow downward trend. When the deformation rate is 5 s^{-1} , the change in the flow stress decreases rapidly and linearly with the increase in temperature, and the change is more obvious.

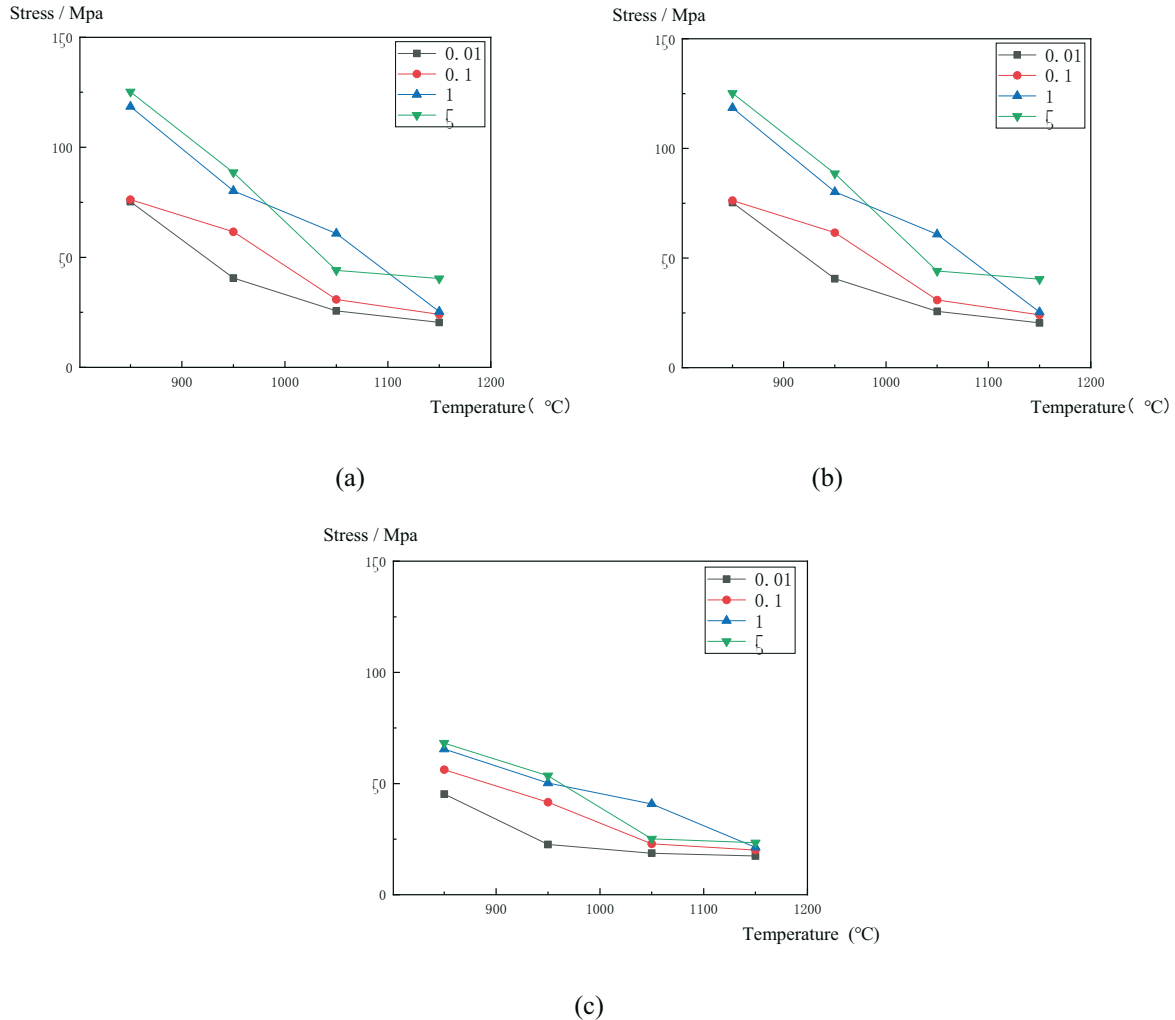


Fig. 6 Relationship curves between flow stress and deformation temperature under different true strains
(a) 0.3 MPa (b) 0.6 MPa (c) 0.9 MPa

In conclusion, the influence of the flow stress cannot be ignored in the analysis of the stress-strain curves under different conditions. Therefore, the effects of strain rate $\dot{\epsilon}$, deformation temperature T and deformation ϵ , as well as the flow stress should be considered when the material is hot compressed in the Gleeble-3800 thermal simulator.

3.2 Constitutive analysis

3.2.1 Selection of a constitutive model

During the hot compression of metallic materials in a Gleeble-3800 thermal simulator, the strain rate, deformation temperature T and deformation ϵ are often affected. According to literature, the widely used models to describe metal thermal shrinkage include the Johnson-Cook flow stress model [26, 27], the constitutive equation model based on the Arrhenius hyperbolic sine function [28, 29] and the normalized Cockcroft & Latham damage model [30, 31, 32]. The Johnson-Cook model can take into account the effect of strain rate, deformation temperature and deformation amount on the flow stress of metallic materials and can effectively predict the mechanical behaviour in the large range of strain rates and temperatures.

The phenomenology-based Johnson-Cook (J-C) model has achieved great success mainly due to its simple multiplication form and excellent ability to predict the strain rate and the mechanical behaviour in a temperature range. In addition, the J-C model is composed of strain rate, strain hardening and temperature, its form is very suitable for finite element simulation and verification, and can also provide a good foundation for subsequent damage theory research and secondary development simulation.

However, no single constitutive model is perfect and can apply to all complex types of conditions. In the original form of the J-C model, the computational temperature requirement is above the lowest experimental temperature. In other words, the application range of the J-C model is only limited to the lowest experimental temperature. Therefore, it is particularly important to correct the temperature term of the J-C model to accurately predict the thermal deformation behaviour at a low temperature. To overcome this drawback, the J-C model is improved, and the improved model can be used even with the calculated temperature below the reference temperature.

3.2.2 Establishing the constitutive equation

Johnson-Cook [33, 34, 35, 36] proposed a phenomenological constitutive model applicable to metals under strain, strain rate and different temperatures. The specific expression of this constitutive model is:

$$\sigma = (A + B\varepsilon^n)(1 + C \ln \dot{\varepsilon}^*)(1 - T^{*m}) \quad (3)$$

where A is the initial yield stress; B is the strain hardening modulus of the material; C is the strain rate strengthening parameter of the material; n is the strain hardening coefficient; σ is the equivalent stress; ε is the equivalent strain; $\dot{\varepsilon}^* = \dot{\varepsilon}/\dot{\varepsilon}_0$ is the dimensionless strain rate ($\dot{\varepsilon}_0$ usually 1.0 s^{-1}). In Eq. (3), the expression in the first set of parentheses gives the strain dependence; the second set of parentheses gives the instantaneous strain rate sensitivity; the third term shows the relationship between stress and temperature.

T^* is the dimensionless temperature and is defined as:

$$T^* = \frac{T - T_r}{T_m - T_r} \quad (4)$$

where T_r is the indoor reference temperature and T_m is the melting point temperature of metallic materials. In the temperature term, m is usually a decimal number, so T_r must be selected as the lowest temperature or the lowest experimental temperature, T is the current temperature, and Eq. (3) is valid only when $T \geq T_r$. Due to the temperature term, the original J-C model is not suitable for calculating the flow stress of metals at $T < T_r$.

When the strain rate is high, the temperature change caused by plastic deformation cannot be ignored. Referring to the dynamic experimental data, the adiabatic temperature rise caused by plastic deformation estimated by the stress-strain curve can be expressed as:

$$\Delta T = \frac{\beta}{\rho C_p} \int_0^{\varepsilon^p} \sigma(\varepsilon^p) d\varepsilon^p \quad (5)$$

where β is the coefficient of plastic work converted to heat; ρ is density; C_p is the heat capacity at constant pressure.

Based on the presented above, the original J-C model cannot calculate the flow stress when $T < T_r$. Although some improved J-C models can calculate the flow stress, they still have some fitting parameters in the temperature term, which still cannot make an accurate prediction.

3.2.3 Modification of the constitutive model

Based on the research results presented above, the researchers [37, 38] proposed a model considering the influence of temperature on the yield strength of materials from the perspective

of energy. This mode is based on the equivalence relation between thermal energy and distortion energy. According to the contribution of elastic deformation energy and corresponding thermal energy to yield strength, it is assumed that they have equivalent relation at T point. Under the assumed condition, the critical productivity density is given as:

$$W_{\text{total}} = W_d (T) + kW_T (T) \quad (6)$$

where W_{total} is the maximum constant value of the maximum energy storage related to yield strength, $W_d (T)$ and $W_T (T)$ are the work done by construction and heat transfer respectively, T is temperature ($^{\circ}\text{C}$), k is the ratio coefficient of strain energy and heat energy.

Researchers presume that there is an equivalent relationship between potential energy and atomic kinetic energy. Therefore, the later generations [39] proposed a new yield strength model related to temperature, whose simplified form is:

$$\sigma_y(T) = \left[\frac{(1+\mu_{T0})}{(1+\mu_T)} \cdot \frac{E_T}{E_{T0}} \cdot \frac{T_m-T}{T_m-T_0} \right]^{0.5} \sigma_y(T_0). \quad (7)$$

Eq. (7) establishes the quantitative relationship among yield strength, Poisson's ratio and Young's modulus at any temperature. The temperature effect is mainly manifested in Poisson's ratio and Young's modulus, both of which are related to temperature. Also, E_T and μ_T can be easily found in manuals or literature on materials. In addition, the model has no temperature limit and can be used even if the current temperature is below the reference temperature.

Since the above formula proposed the equivalent theory of heat energy and twisting strain energy, and considered the influence of temperature on Poisson's ratio and Young's modulus, the temperature term in the original J-C model is substituted into Eq. (7), and the theory is considered to be effective. In addition, it does not introduce new material constants.

Based on the above discussion, an improved J-C model is proposed to study the plastic response over a wide temperature range, irrespective of the current temperature being above or below the reference temperature. The flow stress is expressed as:

$$\sigma = (A + B\varepsilon^n)(1 + C \ln \dot{\varepsilon}^*) \left[\frac{(1+\mu_{T0})}{(1+\mu_T)} \cdot \frac{E_T}{E_{T0}} \cdot \frac{T_m-T}{T_m-T_0} \right]^{0.5} \quad (8)$$

Therefore, a new modified Johnson-Cook model without fitting parameters is established. In the improved J-C model, A , B , n and C are the model parameters to be determined. E_T is the elastic modulus at temperature (T); T_0 is usually used as room temperature; E_{T0} is the elastic modulus at room temperature. Using this method, the flow stresses of metals at high and low temperatures can be described or predicted. This modified Johnson-Cook model is not easily measured experimentally.

3.3 Establishing the hot working diagram

3.3.1 Introduction to hot working diagram

The hot working diagram is an important tool to optimize the hot working process. It can record the plastic deformation capacity of metallic materials under different thermal deformation conditions (deformation temperature, strain rate, strain variable). The safe zone (such as dynamic recrystallisation zone) and the dangerous zone (such as cavity zone and grain boundary crack zone) of plastic processing can be determined by using the hot working diagram, so as to rationally formulate the hot working process of materials and accurately control the microstructure of materials.

At present, the thermal processing diagram is mainly expressed based on two models. One is the thermal processing diagram based on an atomic model, such as the Raj processing diagram. The other is the hot working diagram based on the dynamic materials model

(DMM). The Raj processing diagram based on atomic model has limitations in practical application and cannot be used for alloy materials with complex structure. Therefore, the DMM hot working diagram, which is superimposed by the energy dissipation diagram and the instability diagram, has become the most popular hot working diagram at present.

3.3.2 Obtaining the parameters of the hot working diagram

Before establishing the DMM hot working diagram, the parameters to be obtained are: (1) deformation temperature T ; (2) strain rate $\dot{\epsilon}$; (3) peak stress σ ; (4) strain rate sensitive index m ; (5) dissipation rate factor η ; (6) instability criterion ξ . Strain rate sensitive index m , dissipation factor η and instability criterion ξ need to be calculated later. According to the relevant literature and related papers, the calculation formula for solving these parameters is obtained.

The strain rate sensitive index m can be calculated as follows:

$$m = \frac{\partial \ln \sigma}{\partial \ln \dot{\epsilon}} \quad (9)$$

where σ is the peak stress, $\dot{\epsilon}$ is the strain rate.

The formula for the calculation of dissipation factor η is as follows:

$$\eta = 2 \left(1 - \frac{1}{1+m} \right) = \frac{2m}{1+m} \quad (10)$$

where m is the parameter value obtained in Eq. (9). The higher the value of η is, the more power dissipated for microstructure evolution, the better the machinability of the material will be. Therefore, in the hot working diagram, the higher the value of η is, the better the machining performance is.

The formula for calculating the instability criterion ξ is:

$$\xi (\dot{\epsilon}) = \frac{\partial \ln \frac{m}{m+1}}{\partial \ln \dot{\epsilon}} + m < 0 \quad (11)$$

So far, all the parameters required for drawing the hot working diagram can be calculated, and the obtained data is shown in Table 5.

Table 5 Data needed for heat processing map generation

T (°C)	$\dot{\epsilon}$	$\ln \dot{\epsilon}$	σ	$\ln \sigma$	m	η	$\ln \frac{m}{m+1}$	ξ
850	0.01	-4.605	115.29	4.83	0.31	0.47	-1.44	-0.46
850	0.1	-2.303	135.23	5.04	0.23	0.38	-1.67	-0.71
850	1	0	168.49	5.29	0.09	0.17	-2.46	-2.06
850	5	1.609	180.2	5.31	0.03	0.07	-3.42	-3.15
950	0.01	-4.605	60.57	4.10	0.88	0.94	-0.76	-0.15
950	0.1	-2.303	91.58	4.71	0.85	0.69	-1.07	-0.96
950	1	0	120.24	4.98	0.10	0.18	-2.42	-2.61
950	5	1.609	138.52	5.00	0.03	0.06	-3.47	-3.46
1050	0.01	-4.605	45.68	4.02	0.10	0.19	-2.36	-0.19
1050	0.1	-2.303	55.87	4.09	0.09	0.17	-2.45	0.59
1050	1	0	80.84	4.23	0.27	0.43	-1.55	1.55
1050	5	1.609	84.11	4.54	0.45	0.63	-1.16	1.74
1150	0.01	-4.605	40.42	3.75	0.05	0.10	-3.01	1.98
1150	0.1	-2.303	44.08	3.79	0.10	0.18	-2.43	1.85
1150	1	0	55.35	4.01	0.37	0.54	-1.32	1.70
1150	5	1.609	68.37	4.42	0.59	0.74	-0.99	1.67

3.3.3 Hot working diagram analysis

Origin software is used to analyse and process the data, and the power dissipation diagram and the instability diagram are drawn and then superpositioned to obtain the hot working diagram, as shown in Fig. 7.

Fig. 7 shows the hot working diagram of the LZ50 axle steel at strain temperatures from 850 to 1,150 °C and strain rates from 0.01 to 5 s⁻¹. As can be seen from Fig. 7, the unstable area expands with an increase in the true strain (see the light grey area in the figure). Instability of the LZ50 axle steel is easy to occur when the strain temperature is from 850 to 1,050 °C and the strain rate is from 0.01 to 5 s⁻¹. In addition, under this condition, the material properties of metallic materials are unstable, which has a certain hindrance effect on the subsequent processing. When the temperature is from 1,050 to 1,150 °C and the strain rate is from 1 to 5 s⁻¹, the energy dissipation value reaches the maximum. The dynamic recovery and dynamic recrystallisation of the metal are easy to occur in this region, and the hot working performance of the metallic materials is better.

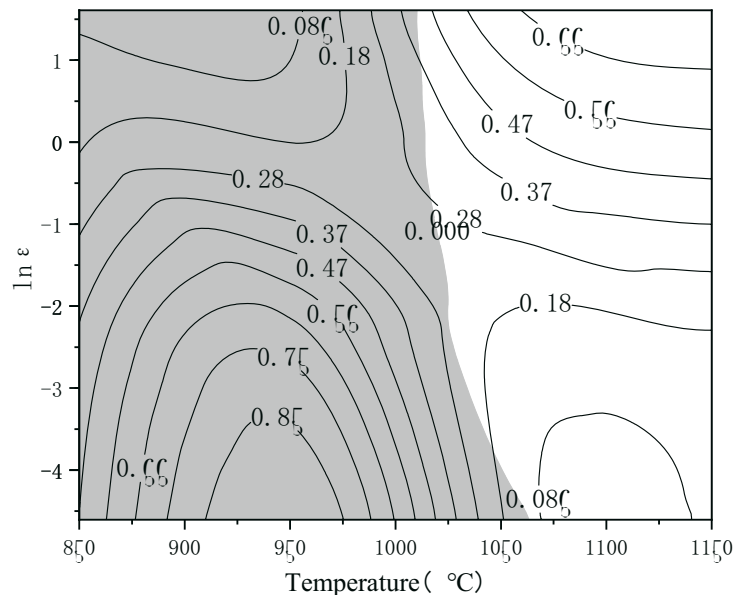


Fig.7 Hot working diagram of LZ50 axle steel

To sum up, the optimal processing range of the LZ50 axle steel is as follows: processing temperature from 1,050 to 1,150 °C, strain rate from 1 to 5 s⁻¹.

3.4 Evolution of the metallographic structure

3.4.1 Metallographic sample preparation

Metallographic sample preparation is the basis for the microstructure observation. This preparation includes sampling, rough grinding, fine grinding, polishing, corrosion and other steps, so that the material fulfills the metallographic observation requirements for the process. Also, the prepared sample must have a clear field of view and real microstructure morphology, which then lays a good foundation for the identification and observation of the microstructure.


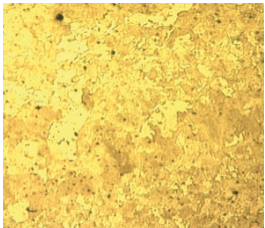
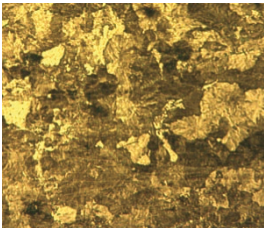
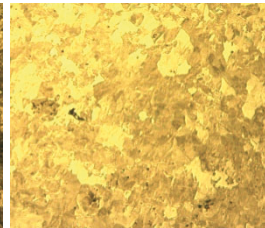

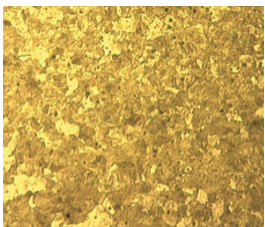

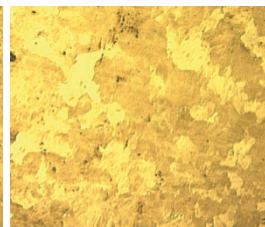
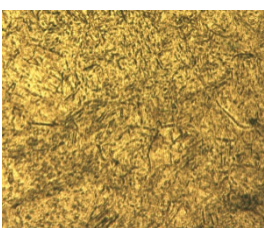

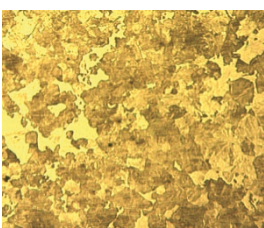
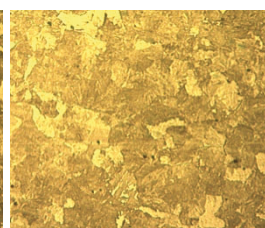
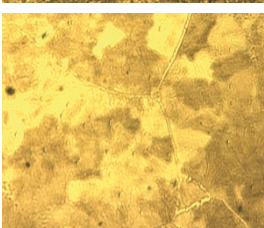
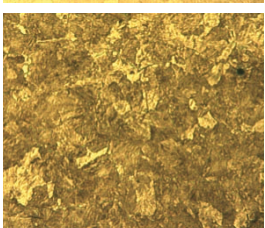
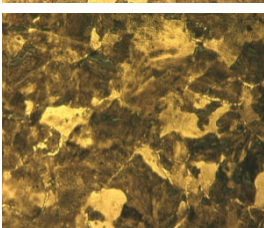
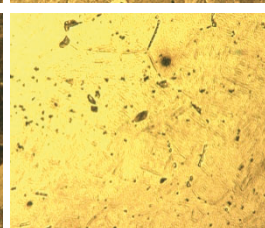
The specific procedure is the following: after the deformation of the sample through line cutting, the semicircular samples will be cut out of the cross section, so that it becomes a sample suitable for the microstructure study. First of all, the surface of the samples is polished on a metallographic sample grinding and polishing machine for the section to get the mirror effect. Secondly, the sample undergoes the corrosion treatment: a cotton ball dipped in a 4% (volume ratio) nitric acid alcohol mixture is used to wipe the corrosion on the surface of the sample,

corrosion time of 10 to 15s is appropriate, and when the sample surface presents a layer of light gray mist film, it is immediately put into alcohol solution for cleaning. Finally, the alcohol on the sample is dried with a hair dryer, and the microstructure of the prepared sample is viewed under a metallographic microscope.

3.4.2 Metallographic microstructure evolution

Table 6 shows the microstructure of the LZ50 axle steel at different strain rates and deformation temperatures. The transverse expression is the microstructure of the LZ50 axle steel under the strain rates of 0.01, 0.1, 1 and 5 s⁻¹, and the longitudinal expression is the microstructure of the LZ50 axle steel under the deformation temperatures of 850 °C, 950 °C, 1,050 °C and 1,150 °C. According to references [40, 41, 42] the metallographic structure of the LZ50 axle steel mainly consists of ferrite and pearlite.

Table 6 Microstructures of LZ50 axle steel at different strain rates and deformation temperatures

	0.01 s ⁻¹	0.1 s ⁻¹	1 s ⁻¹	5 s ⁻¹
850 °C				
950 °C				
1050 °C				
1150 °C				

It is observed that the grain boundary structure of the material is relatively coarse, so it is not suitable for observation under high power microscope. The magnification of 100x is selected, which can not only clearly show the grain structure, but also can perfectly present the material's organizational evolution in the form of pictures.

Upon observation and analysis, it is concluded that the microstructure consists of coarse ferrite particles and layered pearlite grains. Moreover, the pearlite near the ferrite boundary has an obviously higher microhardness, making a barrier. The comprehensive mechanical properties of pearlite are superior to those of ferrite or cementite alone. According to the metallographic observation of the material, the carbon content of 0.53% suggests that the steel

has the ferrite-pearlite microstructure predominately with the pearlite pseudo phase. The pictures in Table 6 also suggest this fact. The brown coloured grains are pearlite grains. This can be observed with magnifications above 200x and higher.

According to the literature, the mean carbon content of pearlite is 0.77%, and the carbon content of ferrite is low being 0.0218%. Therefore, the content of pearlite and ferrite in the Fe-C carbon steel can be calculated according to the leverage law algorithm:

$$\text{Pearlite content: } W_p = (0.53 - 0.0218) / (0.77 - 0.0218) \times 100\% = 67.923\%$$

$$\text{Ferrite content: } W_f = (0.77 - 0.53) / (0.77 - 0.0218) \times 100\% = 32.077\%$$

In summary, in the LZ50 axle steel with a carbon content of 0.53%, pearlite accounts for 67.923% and ferrite accounts for 32.077%. Obviously, the proportion of pearlite is much larger than that of ferrite.

Upon observation and analysis of the metallography, it can be seen that the dynamic recovery between grains occurs when the deformation rate is constant and the temperature is low (850 °C), resulting in the shortening of deformation time and incomplete recrystallisation. Therefore, the grain size is relatively small. And, at a lower temperature, the hot working of metallic material is not conducive to the later thermal processing of the material. With an increase in temperature, dynamic recrystallisation occurs between grains, which makes the grain size appear coarse, and the hot working of metallic material is not conducive to the homogenisation and processing of the material structure. Therefore, a moderate deformation temperature should be selected for the LZ50 axle steel during hot working. The comprehensive comparison and analysis have shown that it is more appropriate to choose the deformation temperature of 1,050 °C.

Under the condition of a constant deformation temperature and a low deformation rate (0.01 s^{-1}), the flow stress is low, the dynamic recrystallization of grains is presented at this time, and the grains are relatively coarse. As the strain rate increases, the grains do not have enough time to nucleate and grow. Therefore, when the strain rate is too high, the grains appear to be refined.

4. Conclusion

The stress-strain curve was obtained by performing a thermal compression test on the LZ50 axle steel by using a Gleeble-3800 thermal simulator at different deformation temperatures and strain rates, then a suitable constitutive equation was established using the obtained data and variables, and the optimal process area of heat deformation was predicted using the heat processing map. Finally, another metallographic analysis of the compressed samples investigated the microstructural evolution at different strain rates and temperatures. The main conclusions are as follows:

(1) In the process of hot compression forming, the true stress of the LZ50 axle steel increases rapidly at the initial stage, then decreases at the middle stage, and gradually flattens at the later stage.

(2) The Johnson-Cook model can effectively predict the mechanical behaviour in the large strain rate and temperature range by considering the effect of strain rate, deformation temperature and deformation amount on the flow stress of metallic materials when analysing and applying the constitutive model to the deformation factors affecting the deformation of the LZ50 axle steel.

(3) Based on the established hot working diagram, the optimal process range of the LZ50 axle steel is as follows: the optimal processing temperature ranges from 1,050 to 1,150 °C, and the optimum strain rate ranges from 1 to 5 s^{-1} .

(4) When the deformation rate is constant, the grain size appears coarse with an increase in the deformation temperature. When the deformation temperature is constant, the grain size is refined with an increase in the deformation rate.

Declaration of competing interest

The authors declare that they have no known competing financial interests or personal relationships that could influence the work reported in this paper.

Acknowledgements

This work is supported by the National key research and development programmes of China (Grant No. 2018YFB1307902) and the Shanxi Provincial Science and Technology Platform Project (Grant 201805D121006).

REFERENCES

- [1] Lu Shujuan. Study on the fatigue life prediction method of axle materials based on crystal plastic finite element. Beijing Jianzhu University, 2020.
- [2] Li Chengbin, Liu Jun, Jiang Peng. Analysis of EA1N. *Continuous casting*, 2020,232 (6):57-61,67.
- [3] Huang Wen, Zhang Yan, Li Dezhi, et al. Organization and Mechanical properties of DZ1, 25CrNiMo, and 30CrNi3MoV axle steel. *Metal heat treatment*, 2019,44 (1): 113-117.
- [4] Bing Yang, Yong Xiang Zhao. Experimental research on dominant effective short fatigue crack behavior for railway LZ50 axle steel. *International Journal of Fatigue* 35 (2012) 71-78.
<https://doi.org/10.1016/j.ijfatigue.2010.11.012>
- [5] Yang Dawei, Li Wei, Lin Yingying, et al. Thermal deformation behavior and constitutive model of PH13-8Mo Steel. *Forging and pressing technology*,2021,46 (5): 234-239,260.
- [6] Jin Xueqin, Zhang Jian, Bi Dasheng. Digital Simulation of thermal compression dynamics of P91 steel. *Forging Technology*, 2012,37 (3): 119-122,126.
- [7] Zhang Yonggang, Dang Jinhua, Li Hongbin. Gleeble Compression Test Friction Correction Study. *Thermal Processing Process*, 2014,43 (12): 120-122.
- [8] Sun, Kong De Lei, Lei Liping-Microsimulation of typical forging process. *Forging Technology*, 2021,46 (6): 33-40.
- [9] Wu Shuting, Feng Wei, Cao Jichang, et al. Study of the deformation behavior and microorganization of 20CrMnTiH steel. *Thermal processing process*, 2014, 43 (16): 105-108,111.
- [10] C.J. Bennetta, S.B. Leen, E.J. Williams, et al. A critical analysis of plastic flow behaviour in axisymmetric isothermal and Gleeble compression testing. *Computational Materials Science* 50 (2010) 125-137. <https://doi.org/10.1016/j.commatsci.2010.07.016>
- [11] Ahmad Chamanfar, Mohammed T. Alamoudi, Nicholas E. Nanning, et al. Analysis of flow stress and microstructure during hot compression of 6099 aluminum alloy (AA6099). *Materials Science & Engineering A* 743 (2019) 684-696.
- [12] Y. Gajalappa, A. Krishnaiah, K. Basanth Kumar, et al. Flow behaviour kinetics of Inconel 600 superalloy under hot deformation using gleeble 3800. *Materials Today: Proceedings* 45 (2021) 5320-5322.
<https://doi.org/10.1016/j.matpr.2021.01.909>
- [13] H. Xiao, X.G. Fan, M. Zhan, et al. Flow stress correction for hot compression of titanium alloys considering temperature gradient induced heterogeneous deformation. *Journal of Materials Processing Tech.* 288 (2021). <https://doi.org/10.1016/j.jmatprotec.2020.116868>
- [14] Qiang Li, Biao Guo, Xiao Li, et al. Fracture prediction of powder metallurgical Fe-Cu-C steel at elevated temperatures via finite element-aided hot tensile tests. *journal of materials research and technology* 2021;12 : 423 -436. <https://doi.org/10.1016/j.jmrt.2021.03.008>
- [15] Kun Doua, Qing Liu. Hot deformation behavior and constitutive modelling of low carbon micro-alloyed steel YQ450NQR1 during isothermal compression. *Mechanics of Materials* 148 (2020).
<https://doi.org/10.1016/j.mechmat.2020.103430>
- [16] S.H. Adarsh, V. Sampath. Hot deformation behavior of Fe-28Ni-17Co-11.5Al-2.5Ta-0.05B (at.%) shape memory alloy by isothermal compression. *Intermetallics* 115 (2019).
<https://doi.org/10.1016/j.intermet.2019.106632>

- [17] Baohui Tian, Siegfried Kleber, Silvia Schneller, et al. Influencing factors of global and local deformation in hot compression. *Procedia Manufacturing* 15 (2018) 381-387. <https://doi.org/10.1016/j.promfg.2018.07.233>
- [18] X. Wang, H. Lia, K. Chandrashekhar. Inverse finite element modeling of the barreling effect on experimental stress-strain curve for high temperature steel compression test. *Journal of Materials Processing Technology* 243 (2017) 465-473. <https://doi.org/10.1016/j.jmatprotec.2017.01.012>
- [19] D.J. Yu, D.S. Xu, H. Wang. Refining constitutive relation by integration of finite element simulations and Gleeble experiments. *Journal of Materials Science & Technology*, 2019, 35(6): 1039-1043. <https://doi.org/10.1016/j.jmst.2018.12.026>
- [20] J.F. Zheng, J. Luo, J.L. Mo. Fretting wear behaviors of a railway axle steel. *Tribology International* 43 (2010) 906-911. <https://doi.org/10.1016/j.triboint.2009.12.031>
- [21] Zhibiao Xu, Jinfang Peng, Jianhu Liu, et al. Study on fretting wear and tribo-chemical behavior of LZ50 axle steel in torsional fretting fatigue. *Wear* 426-427 (2019) 704-711. <https://doi.org/10.1016/j.wear.2018.12.074>
- [22] LiuShun, XuMang, LiTianrui, et al. Thermal deformation behavior of high-strength corrosion-resistant Ti80 alloy and tissue properties of hot-rolled sheet materials. *Rare Metal Materials and Engineering*, 2021, 50 (9): 3203-3212.
- [23] Wang Shun. 2205 Dual-phase stainless steel / Q345 Carbon Steel Thermal compression Composite Process and Microorganization evolution. Taiyuan University of Science and Technology, 2020.
- [24] Lv Zhenhua. Research on the formation of 42CrMo Steel. Taiyuan University of Science and Technology, 2015.
- [25] Liu Hao. 38CrMoAl Steel Recrystallization Behavior Research. Dalian University of Technology, 2020.
- [26] Ren Jibin. Johnson-Cook configuration model and failure parameters of A 97. *Journal of South China University of Technology*, 2019,47 (8): 137-143.
- [27] Xuemei Wang, Jun Shi. Validation of Johnson-Cook plasticity and damage model using impact experiment. *International Journal of Impact Engineering* 60 (2013) 67-75. <https://doi.org/10.1016/j.ijimpeng.2013.04.010>
- [28] Shuai Yang, Yun Lu, Yangang Guo, et al. Crushing behavior of alumina inclusions with different porosity during hot compression. *Ceramics International* 47 (2021) 6562–6572. <https://doi.org/10.1016/j.ceramint.2020.10.244>
- [29] Gang TAN, Hui-zhong LI, Yan WANG, et al. Hot working characteristics of HEXed PM nickel-based superalloy during hot compression. *Trans. Nonferrous Met. Soc. China* 30(2020) 2709–2723. [https://doi.org/10.1016/S1003-6326\(20\)65414-0](https://doi.org/10.1016/S1003-6326(20)65414-0)
- [30] Du Kexue, Chen Xuewen, Liu Jiaqi, et al. High temperature Normalized Cockcroft & Latham damage model of X12 alloy steel and parameter inversion analysis method of alloy steel. *Journal of Plastic Engineering*, 2021,28 (4): 174-180.
- [31] Zhang Jingli. Determination of the Ti600 alloy critical damage values based on the Normalized Cockcroft & Latham toughness damage criteria. *Material engineering*. 2019,47(7):121-125.
- [32] Zhang Jingli, Chen Xuewen, Liu Zehu. Determination method and test of high temperature critical damage value of 45Cr4NiMoV steel. Zhang Jingli, *Journal of Plastic Engineering*, 2012,19 (3): 44-47.
- [33] G.R. Johnson, W.H. Cook, Fracture characteristics of three metals subjected to various strains, strain rates, temperatures and pressures, *Eng. Fract. Mech.* 21(1985) 31–48. [https://doi.org/10.1016/0013-7944\(85\)90052-9](https://doi.org/10.1016/0013-7944(85)90052-9)
- [34] Ruzhuan Wang , Weiguo Li , Baohua Ji , Daining Fang. Fracture strength of the particulate-reinforced ultra-high temperature ceramics based on a temperature dependent fracture toughness model. *Journal of the Mechanics and Physics of Solids* 107 (2017) 365-378. <https://doi.org/10.1016/j.jmps.2017.07.012>
- [35] Xinyuan Qian, Xuebing Peng, Yuntao Song, et al. Dynamic constitutive relationship of CuCrZr alloy based on Johnson-Cook model. *Nuclear Materials and Energy* 24 (2020). <https://doi.org/10.1016/j.nme.2020.100768>
- [36] Wang Jianjun, Hu Xueyao, Yuan Kangbo, et al. Impact resistance prediction of superalloy honeycomb using modified Johnson-Cook constitutive model and fracture criterion. *International Journal of Impact Engineering* 131 (2019) 66-77. <https://doi.org/10.1016/j.ijimpeng.2019.05.001>
- [37] Yuntian Wang, Xiangguo Zeng, Huayan Chen, et al. Modified Johnson-Cook constitutive model of metallic materials under a wide range of temperatures and strain rates. *Results in Physics* 27 (2021). <https://doi.org/10.1016/j.rinp.2021.104498>

- [38] Weiguo Li, Fan Yang, Daining Fang. The temperature-dependent fracture strength model for ultra-high temperature ceramics. *Acta Mech Sin* (2010) 26:235-239. <https://doi.org/10.1007/s10409-009-0326-7>
- [39] Xianhe Zhang, Weiguo Li, Jianzuo Ma, et al. A novel temperature dependent yield strength model for metals considering precipitation strengthening and strain rate. *Computational Materials Science* 129 (2017) 147-155. <https://doi.org/10.1016/j.commatsci.2016.12.005>
- [40] Y.X. Zhao, B. Yang, M.F. Feng, H. Wang. Probabilistic fatigue S-N curves including the super-long life regime of a railway axle steel. *International Journal of Fatigue* 31 (2009) 1550–1558. <https://doi.org/10.1016/j.ijfatigue.2009.04.016>
- [41] Zhibiao Xu, Jinfang Peng, Jianhua Liu, et al. Investigation of fretting fatigue behavior and micro-structure evolution in LZ50 steel subjected to torsional load. *International Journal of Fatigue* 128 (2019). <https://doi.org/10.1016/j.ijfatigue.2019.06.033>
- [42] Yun Zou, Jingkai Li, Xiao Liu, et al. Effect of multiple ultrasonic nanocrystal surface modification on surface integrity and wear property of DZ2 axle steel. *Surface & Coatings Technology* 412 (2021). <https://doi.org/10.1016/j.surfcoat.2021.127012>

Submitted: 27.11.2021

Accepted: 03.4.2022

Qinhong Fan
Hongwei Gao*
Zhibing Chu
Yuxin Zhang
Yanan Cui
Wenze Wang
School of Mechanical Engineering,
Taiyuan University of Science and
Technology, Taiyuan, Shanxi Province,
China
*Corresponding author:
1059063799@qq.com